Acta Materialia 103 (2016) 534–546

Contents lists available at ScienceDirect

Acta Materialia

journal homepage: www.elsevier.com/locate/actamat

Full length article

In situ X-ray tomographic microscopy of Kirkendall pore formation and evolution during homogenization of pack-aluminized Ni–Cr wires

A.E. Paz y Puente [a,*], D. Erdeniz [a], J.L. Fife [b], D.C. Dunand [a]

[a] Department of Materials Science and Engineering, Northwestern University, 2220 Campus Drive, Evanston, IL, 60208, USA
[b] Swiss Light Source, Paul Scherrer Institute, 5232 Villigen PSI, Switzerland

ARTICLE INFO

Article history:
Received 14 August 2015
Received in revised form 22 September 2015
Accepted 9 October 2015
Available online 6 November 2015

Keywords:
Ni-Al-Cr
Diffusion
X-ray tomography
Kirkendall effect
Microtubes

ABSTRACT

The Kirkendall effect, usually associated with the formation of undesirable fields of micron-size pores, can be used to fabricate hollow nano- and microstructures, where all pores have coalesced into a single cavity. Here, this concept is used with the goal of converting 50 μm diameter Ni-20wt.%Cr wires into Ni–Cr–Al tubes by diffusion of a surface-deposited aluminide coating. The formation and evolution of Kirkendall pores, created by imbalanced diffusion fluxes of Al, Ni and/or Cr, are investigated using both in situ X-ray tomographic microscopy and ex situ annealing studies. The tomography results indicate that the pores nucleate near the interface between the Ni–Cr core and β-NiAl(Cr) reaction layer that develops upon homogenization. They then grow and coalesce near the center of the radial cross-section of the wire. This is followed by a stagnation period until the pores migrate longitudinally due to the influence of a temperature gradient imposed by the laser heating used for annealing. The ex situ experiments are in qualitative agreement with the tomography study with the exception of the secondary pore migration along the wire length, as expected because the ex situ study is conducted under isothermal conditions. Detailed features of the microstructure were discernable only upon metallographic preparation and include Cr-rich precipitates and an α-Cr(Al,Ni) rejection region that formed during coating and homogenization, respectively. In situ X-ray tomographic microscopy is thus demonstrated to be a viable technique to use in conjunction with more conventional ex situ metallographic techniques to conduct interdiffusion and Kirkendall pore studies.

1. Introduction

The Kirkendall effect is a well-established phenomenon, which was discovered in 1947 by Kirkendall and Smigelskas [1]. An important manifestation of this effect is the formation of pores near the interfaces of diffusion-bonded dissimilar materials. These so-called Kirkendall pores form as a result of the discrepancies in atomic fluxes in opposite directions, therefore causing a supersaturation of vacancies on the side of the faster diffusing component [2–6]. Typically, these Kirkendall pores are regarded as detrimental because they can deteriorate the mechanical, thermal, and/or electrical properties of the material. Therefore, the aim is often to prevent or suppress the formation of Kirkendall pores. However, in 2004 [7], this phenomenon was exploited to form hollow nanoparticles where a single pore is formed by interdiffusion of Co and O, S, or Se. Several recent studies have investigated this mechanism, though there are only rare examples of metal–metal reactions forming these structures [3,8,9]. This fabrication route has also recently been extended to nanotube structures [3,10–17]. While several studies involving nano-scaled hollow structures have been conducted, few have been performed at the micro-scale. These include the formation of microshells (hollow spheres) and microcages (hollow cubes or polyhedra) with typical dimensions of 1–30 μm [18–21].

One of the ways that these hollow structures can be achieved is by starting with a dense core–shell structure in which the shell components diffuse slower than the core components, resulting in an inward flux of vacancies toward the center [3,11,14]. Unlike the large number of pores created in diffusion couples with larger volumes, in this case, the pores can coalesce into a single Kirkendall pore due to radial symmetry and spatial confinement. The coating technique used to deposit the shell layer on these nano- or micro-size substrates is critical to ensure a uniform coating. While at the nano-scale the conformity and uniformity of atomic layer deposition (ALD) is required for accurate thickness control, more conventional deposition techniques can be used at the micro-scale, which are faster and more cost effective than ALD [3]. Pack cementation, for example, is a simple chemical vapor deposition

* Corresponding author. Northwestern University, 2220 Campus Dr., Cook Hall 2036, Evanston, IL 60208, USA.
E-mail address: ashleyepyp@gmail.com (A.E. Paz y Puente).

http://dx.doi.org/10.1016/j.actamat.2015.10.013
1359-6454/

(CVD) process that has been used for over a century to deposit coatings with thicknesses spanning a few to a few hundred micrometers [22].

While pack cementation can be used to deposit a variety of elements including Cr [23,24], Ti [25,26] and Mo [27–29], one of the earliest and most common uses is for aluminization. It is still widely used to form protective aluminide coatings on Ni-based superalloy components [30–36] which have been divided into two categories: (i) low temperature, high activity pack deposited coatings and (ii) high temperature, low activity pack deposited coatings [32,37]. In the high activity process, an inward-grown Ni_2Al_3 coating, sometimes with a dispersion of secondary phase precipitates, forms because Al is supplied at a much higher rate than it can react to form β-NiAl; upon further annealing the coating quickly reverts to Al-rich NiAl [37,38]. In addition to these microstructural features, the formation of Kirkendall pores near the surface of the substrate following aluminization of Ni-based alloys has also been observed [38]. Some early work on the binary Ni–Al system also revealed a relatively pronounced Kirkendall effect [39]. Another study investigating the effects of rotational symmetry on the diffusion kinetics and Kirkendall pore formation in Ni-coated Al wires showed that pore coalescence eventually caused the separation of the shell from the core [40]. Furthermore, a more recent study regarding the aluminization of Ni wires and foams illustrates that, upon homogenization, the aluminum-rich coating layer partially separated from the Ni core. This separation was due to the formation of a nearly continuous layer of coalesced Kirkendall pores [41]. The aluminization of pure Ni wires was also studied via phase-field modeling, however, for wires with much less overall Al content such that once homogenized, a $\gamma + \gamma'$ microstructure was reached [42].

Here, we show that, in pack-aluminized Ni-20wt.%Cr wires subjected to homogenization, pores form as a result of the Kirkendall effect and eventually coalesce near the center of the radial cross-section. In this case, size may play an important role as the diameter of the wires, 50 μm, is only somewhat larger than typical Kirkendall pore sizes, usually in the range of 1–25 μm, and therefore spatially confines the growth of the pores. Hence, this fabrication route may be used to create hollow Ni–Cr–Al tubes. We also show via X-ray tomographic methods that pore stagnation followed by rapid pore migration can occur under thermal gradients. This demonstrates that both fast and slow mechanisms are involved, providing insights into possible tailoring techniques for Kirkendall pore microstructures. The present exploration paves the way to extend the Kirkendall method beyond the fabrication of individual tubes to the development of 3D hollow woven and braided structures, which offer lower density, higher specific mechanical properties, and higher surface area than non-hollow wires, making them good candidates for structural applications (e.g., as cores of sandwiches) and thermal applications (e.g., as heat exchangers and catalytic substrates) in hot, oxidative environments [30,43].

2. Experimental Procedures

2.1. Pack aluminization

The samples examined in this study were nichrome wires, acquired from Alfa Aesar (Ward Hill, MA) with an initial diameter of 50 μm and a nominal composition of Ni–20Cr–1Si-0.5Fe (wt.%). These wires were subsequently aluminized, which partially consumes the nichrome core as the aluminide diffusion coating forms, resulting in a core/shell structure having an as-coated diameter ranging between 70 and 80 μm depending upon the amount of Al deposited on each particular wire. The aluminization pack had a composition of 82 wt.% of 20–50 μm Al_2O_3 filler powders, 15 wt.% of <150 μm Raney Ni precursor (Ni-50wt.%Al alloy or Ni-68.5at%Al) source powders, and 3 wt.% 100 μm NH_4Cl activator powders, all of which were procured from Alfa Aesar. Such a pack, labeled P50 in a prior publication [30], has been established previously as a high activity pack because it has greater than 60 at% Al [35]. This powder mixture was mechanically mixed for ~30 min before approximately 25 g was poured into an alumina crucible in two stages with 12 wires, each about 4 cm in length, embedded between the two layers of pack. An alumina lid was then placed on the crucible, which was subsequently mounted on a stage in the water-chilled end of a preheated tube furnace to prevent premature activation of the pack while it was flushed with Ar for 15 min. After flushing, the crucible was inserted into the hot zone of the tube furnace and, after a predetermined time, was retracted back into the water-chilled zone to cool before removing it from the furnace completely. The coating time and temperature were 7 min and 1000 °C, respectively, chosen based on previous experimental results with P50 packs [30]. The aluminized wire specimens were then removed from the pack, ultrasonically cleaned in acetone for ~5 min to remove any pack powders from the surface, and prepared for further processing and characterization.

2.2. Homogenization study via in situ X-ray tomographic microscopy

A set of in situ experiments was conducted at the TOMCAT beamline of the Swiss Light Source at the Paul Scherrer Institut, permitting the observation of the pore development in real-time through laser-based heating [44]. Because the coating thickness can change slightly from wire to wire, which can affect the resulting phase and pore evolution, the in situ tomographic imaging capabilities provide non-destructive knowledge of the initial coating thickness and uniformity and allow observation from a known starting point, unlike the more conventional ex situ diffusion studies. A schematic of the most relevant components of the experimental setup is shown in Fig. 1. The wire sample was encapsulated in a quartz capillary under vacuum and then inserted into an alumina sleeve; this was then mounted to the rotation stage with a stainless steel sample holder. Data were collected using monochromatic X-rays at an energy of 21.5 keV and a pco.EDGE camera mounted to a standard microscope with 20 × magnification (0.325 μm/px). An initial scan was collected at ambient temperature to obtain the thickness of the aluminide coating. Then the laser-based system, utilizing a pyrometer to measure the temperature, was used to heat the sample to a nominal temperature of 1000 °C as the wire was rotated continuously [44]. 1501 projections over 180° of rotation were collected in approximately 2 min (100 ms/projection). Scans were interspersed with a relatively short user-defined sleep time of 3 min in an aim to capture detailed features of the pore evolution. All data were reconstructed using the gridrec algorithm as in Ref. [45]. The pores observed in the resulting reconstructions were then segmented in ImageJ [46] and visualized in 3D using a contour plot in VisIt [47], an open source reconstruction tool available through Lawrence Livermore National Laboratory. For several time steps, a MATLAB script was used to estimate the pore volume fraction; this was done by segmenting the pore and wire areas separately and subsequently summing the pore area over the total wire length. All of the tomography results presented and discussed in the following sections are from two different samples that were aluminized using the same conditions (7 min at 1000 °C) and then subsequently heat-treated during in situ tomographic imaging at the same nominal temperature of 1000 °C.

2.3. Homogenization study via ex situ metallography

The in situ tomographic microscopy results were verified by a series of ex situ isothermal experiments conducted on multiple wires

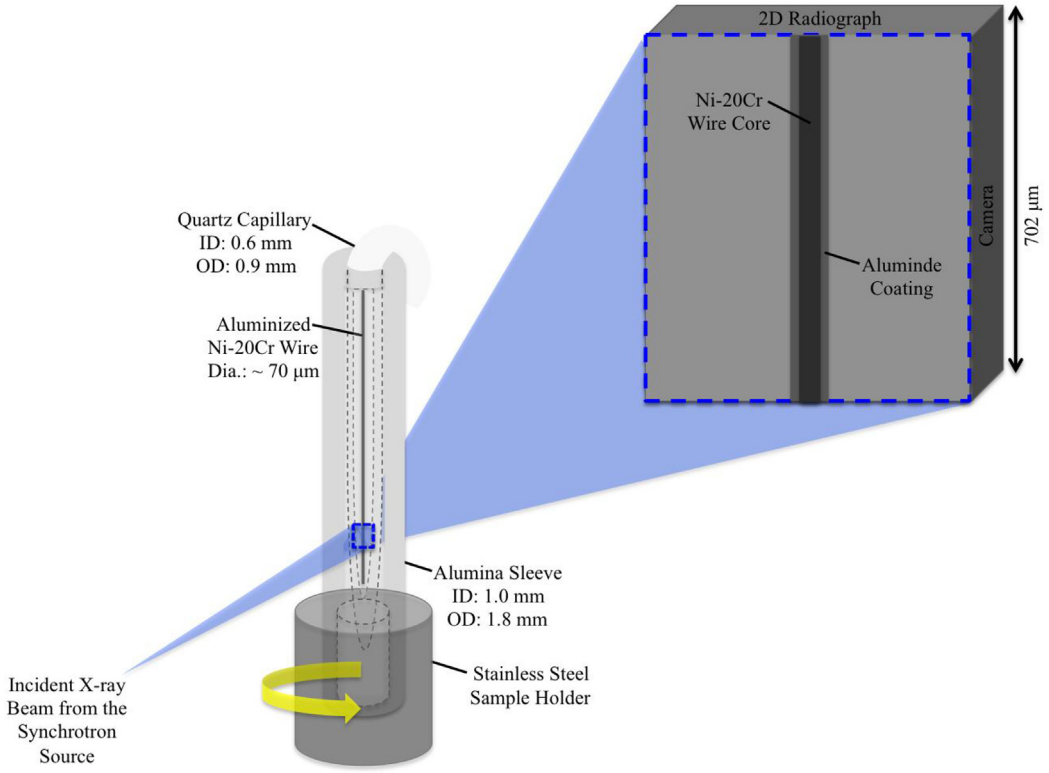

Fig. 1. Schematic of the relevant components of the X-ray tomographic microscopy setup at the TOMCAT beamline of the Swiss Light Source.

using conventional heat treatment and metallographic characterization techniques. The same pack aluminization conditions (7 min at 1000 °C) that were used in the in situ experiments were also used to form the aluminide coating on these wires. However, the ex situ annealing conditions were not the same as in the tomography experiments because it was determined that the wire could react with the quartz capillary if in direct contact. To avoid this interaction, the wires were embedded in Al_2O_3 powder and wrapped in stainless steel foils before encapsulation. Once encapsulated, the wire samples were annealed at 900, 1000, and 1100 °C in a box furnace for a variety of times ranging from 15 min to 16 h. After water-quenching the capsules, the wires were removed from the foil wraps, cleaned in acetone, mounted in epoxy, and polished to 0.05 µm alumina. The microstructure and composition of multiple cross-sections were characterized metallographically for each annealing condition via a combination of optical microscopy (OM), scanning electron microscopy (SEM), and energy dispersive X-ray spectroscopy (EDS). While it cannot be definitively confirmed, the above-mentioned interaction between the quartz and the sample does not appear to have occurred during, or affected the results of, the tomography experiments because the segments of the wire analyzed here were not in direct contact with the capillary as observed in the resulting tomographic images.

3. Results and discussion

3.1. Phase evolution during homogenization

To analyze the microstructural evolution of the aluminized Ni–Cr wires, it is important to know the as-coated microstructure. As shown in Fig. 2, the as-coated wires exhibit a core/shell structure. Based on the reconstructed slice shown in Fig. 2(a), the 15 µm thick shell and the 42 µm diameter core (overall as-coated diameter of 72 µm) both appear to be single-phase. However, Fig. 2(b) clearly illustrates that the shell is a two-phase layer, which consists of chromium-rich precipitates (likely $Cr_{9.5}Al_{16}$ based on the ternary isotherm [48], but labeled Cr_xAl_y) in a nickel aluminide matrix (Ni_2Al_3, as expected for this pack [30] and as confirmed via EDS on polished cross-sections and via XRD on crushed as-coated wires), while the core is indeed single-phase γ-Ni(Cr). Because of the relatively sharp color difference in the metallographic cross-section (Fig. 2(b)), there seems to be two distinct shell layers (marked i and ii). However, the coating is indeed one continuous layer and this appearance is the result of a radial gradient in the chromium-rich precipitate size. An explanation for this gradient could be the preferential coarsening of the Cr-rich precipitates formed earliest near the surface, giving them more time to coarsen as the diffusion front moved toward the wire center. Alternatively, this could be caused by a changing Cr supersaturation due to Cr rejection from the core as the wire homogenizes. During the early stages, coarse precipitates form as a result of an initially low Cr supersaturation, but as Cr continues to be rejected, supersaturation increases and finer precipitates form.

Upon annealing, a diffusion reaction occurs between the shell and the core as the wire homogenizes toward its equilibrium microstructure. The microstructural evolution of a single wire cross-section is presented in Fig. 3 as a series of two-dimensional (2D) tomograms taken from the top of the reconstruction volume. After only 15 min of aging, an intermediate reaction layer forms between the shell and the core. Based on the phase diagram, this layer is expected to be B2–NiAl(Cr). This layer grows at the expense of both the outer layer and the γ-Ni(Cr) core from 15 to 60 min. Finally, after approximately 60 min, the wire appears to be fully homogenous, with the exception of the presence of a large internal pore, appearing after 25 min, which is discussed further in Section 3.2.

To further understand the microstructure evolution during homogenization along the length of the wire within the field-of-view (FOV), Fig. 4 presents a series of 2D radiographs as a function of annealing time. After 15 min, the shell has grown at the expense

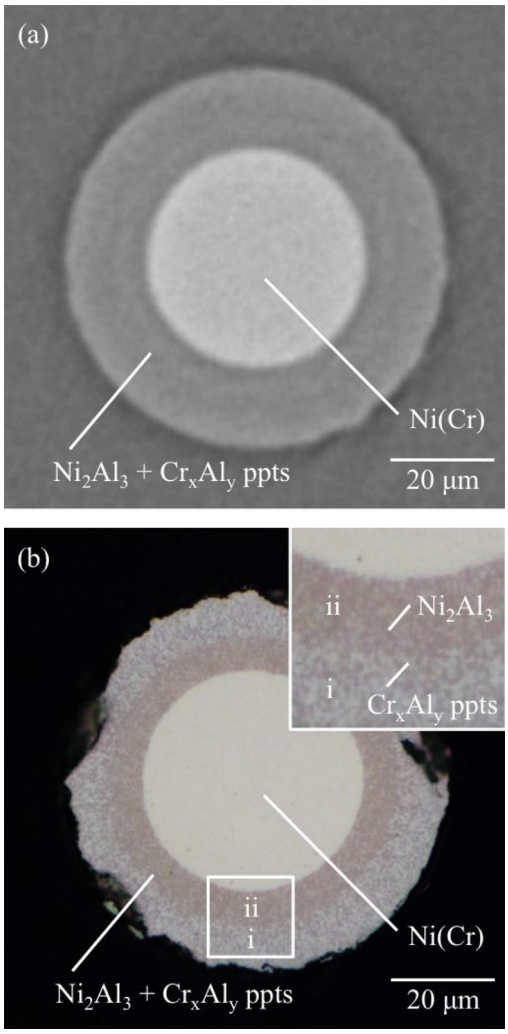

Fig. 2. As-coated aluminized Ni-20wt.%Cr wires shown as (a) a 2D tomographic slice and (b) an optical micrograph with a magnified view of the shell layer in the inset. The edge damage in (b) is due to metallographic preparation.

of the core. By 30 min the top portion of the wire appears to be fully homogenized while the shell/core structure remains visible near the bottom. Also, the formation of pores is observed near the top of the wire (arrows in Fig. 4 starting at 30 min). It is apparent that diffusion occurs faster at the top of the wire than at the bottom, as discussed further in Section 3.2.2, which indicates that a longitudinal thermal gradient is present. However, the magnitude of any temperature gradient using lasers as a mode of heating is experiment-specific and determined by many factors, including the ability of the sample (materials) to couple with the lasers, the temperature range examined, the thermal conductivity of the sample, as well as the overall stability of the experimental setup at temperature. Thus, the same temperature gradients observed by these authors would not necessarily be observed in other experiments.

3.2. *Kirkendall pore evolution during homogenization*

3.2.1. *In situ tomographic microscopy experiments*

3.2.1.1. Equiaxed pores. Kirkendall pore formation and evolution can be observed in the 2D slices in Fig. 3. The initial signs of pore formation, within the resolution limit of the tomography scans (~1 μm), are observed after approximately 25 min of heating as a cavity with a crescent-like cross-section takes shape and grows until it reaches a near-elliptical shape after 60–90 min. There is little change in terms of the pore cross-sectional shape and size between 90 and 240 min, but then the pore begins to grow again. After 285 min, the pore has a nearly circular cross-section as shown in the bottom right image in Fig. 3. The existence and subsequent evolution of these pores along the entire length of the wire in the FOV is even more apparent in the radiographs shown in Fig. 4. The laser position was at the top of the FOV, indicated by a crack in the alumina sleeve (i.e., the almost white line spanning the diameter of the sample marked with an L) that becomes visible on the 15 min projection. Within 30 min, internal pores have started forming in the laser path. After 45 min, pore formation is even more obvious near the top of the FOV and extends to the white dotted line near the center of the FOV. By 90 min, a discontinuous string of pores has developed along the length of the wire within the FOV. This string of pores appears to remain relatively stagnant for another two and a half hours, as illustrated by comparing individual pore shapes and sizes, marked with arrows in Fig. 4. This is unexpected as it was anticipated that the pores would evolve relatively quickly at this high temperature by coalescing and/or sintering to reduce the internal surface area. One possible explanation for this long stagnation is that an oxide scale formed on the interior surface of the pores (e.g., via oxygen penetration into the wire through grain boundary diffusion), which must break up before pore coalescence, migration or sintering can occur. Another hypothesis is that the pores are gas-filled. It has been demonstrated that oxygen can penetrate relatively large distances, e.g., 250 μm after 200 h air exposure at 1000 °C, into polycrystalline Ni alloys via grain boundary diffusion and react with impurity levels of carbon to form carbon di- or monoxide gas bubbles [49,50]. However, it has been determined that high, ~22 wt.%, Cr levels can reduce the oxygen activity enough to prevent this mechanism [50].

Just after 4 h of total annealing time, as shown in Fig. 4 at 260 min, the pore string starts to coalesce near the top of the FOV and evolves relatively quickly, in comparison to the overall annealing time, until a single pore with a capped cylindrical structure, indicated by an arrow in the last projection of Fig. 4, is formed. Meanwhile, an apparently pore-free region, which initially formed at 260 min and grows as shown by the series of white dotted ellipses in Fig. 4, is observed below this capped cylindrical pore; however, there may be pores below the resolution limit that are not visible in the images. The migration of pores toward the hot zone is almost certainly due to the longitudinal temperature gradient present in these experiments. This has also been observed experimentally in nuclear oxide fuel systems and verified through phase-field simulations [51]. This also suggests that the large cylindrical pore observed at the end of the experiment (after 285 min at temperature) is a result of a flux of individual vacancies or pores from the region below it, due to the temperature gradient. Therefore, this series of projections can effectively be split into two groups to discuss the mechanisms involved in the pore evolution. Up to about 90 min, pores are forming and growing via the Kirkendall effect where the primary driving force is the radial concentration gradient as the wire undergoes homogenization. Beyond this time, the radial concentration gradient is no longer present as the wire is fully homogenous, and thus, the pores begin to coarsen and eventually migrate longitudinally, likely due to the now dominant driving force of the longitudinal temperature gradient.

While the chronological series of reconstructed slices and projections shown in Figs. 3 and 4, respectively, provide insights in terms of the overall evolution of the pores, it is difficult to distinguish much detail at the pore level. It is more informative to visualize the pores in 3D so that individual features of the pore morphology can be discerned. Fig. 5 shows a time series of 3D reconstructions for the top half of the FOV from 245 min to the end of the experiment at 285 min. With these images, the complex merging and splitting

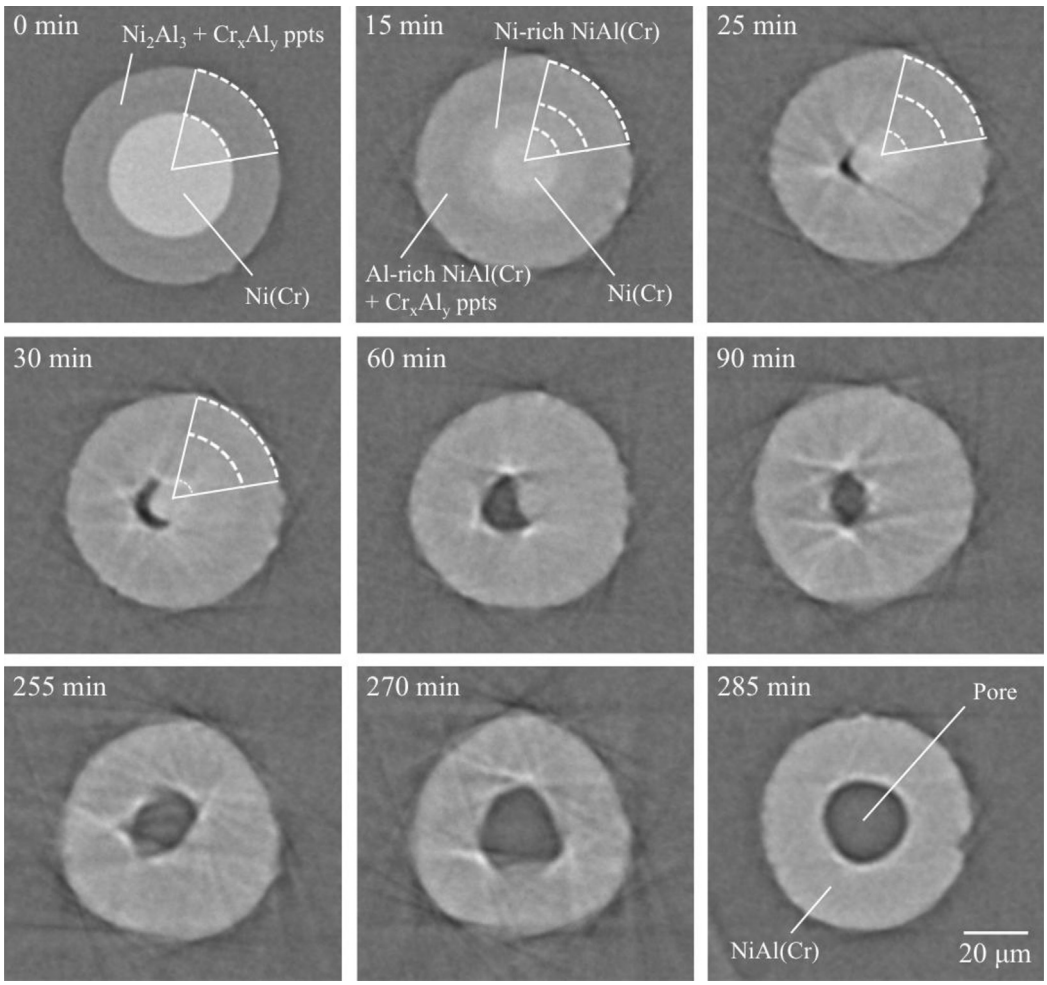

Fig. 3. Time evolution of 2D tomographic slices taken from the top of the reconstruction volume showing phase and pore evolution in the wire. The alternating brighter white/darker black areas seen at the interface between the air gap and the wire and at the edges of the wire are streaking artifacts caused by the difference in X-ray absorption between the air gap and the material and the material and the alumina sleeve, respectively. The streaking is further enhanced by the sample-to-detector distance in the experimental setup and by movement artifacts in certain images (e.g., 90 min and 270 min).

events (examples indicated by the series of arrows labeled (a) and (b), respectively, in Fig. 5) are more visible as the pores evolve under the presence of the temperature gradient.

3.2.1.2. Dumbbell cavity. At the end of the experiment, after the sample had cooled, the sample height was adjusted to center the laser position in the FOV and a final room-temperature scan was taken. The 2D radiograph of the final structure is shown in Fig. 6(a). It is apparent that the capped cylindrical pore formed symmetrically about the laser position (marked with an L, which corresponds to the fracture of the alumina sleeve, as mentioned above) and resulted in a dumbbell-shaped pore. This feature provides further evidence of the presence of a symmetrical longitudinal temperature gradient, which caused the migration of pores toward the highest temperature region of the wire.

At first sight, the dumbbell shape is surprising, as the simpler shape of a cylinder with hemispherical caps of the same diameter as the cylinder is intuitively expected. A possible explanation for the much larger diameter of the spherical caps relies on the concept of constant mean curvature surfaces and, therefore, constant chemical potential surfaces [52]. Measuring the diameters of the cavity tips from reconstructed slices of the dumbbell, the maximum diameter of the spherical cap is approximately 2 times (1.99 and 1.94 for the top and bottom, respectively) that of the diameter of the cylindrical portion, as shown in Fig. 6(b) and (c). The mean curvature is the average of the two principal curvatures of a surface, which are the reciprocals of the principal radii. For a sphere the two principal curvatures are equal and for a cylinder one of the principal curvatures is zero. Thus, given a constant radius, the mean curvature for a sphere is twice that of a cylinder. In order to maintain a constant mean curvature, the radius of a sphere must be twice that of the radius of a cylinder as observed in this dumbbell pore that consists of two spheres connected to a cylinder. Therefore, the dumbbell shape seen in Fig. 6 may represent a constant chemical potential surface, which is at equilibrium in the temperature gradient of the wire.

The 3D reconstruction of the dumbbell pore is presented in Fig. 7(a) along with two higher magnification views of specific features of the dumbbell, including, in Fig. 7(b), small satellite pores that are not clearly visible in the unprocessed 2D projections and, in Fig. 7(c), grain boundaries on the surface of the pore. These features can give some insight into the mechanisms involved in the formation of the dumbbell pore structure. For example, in Fig. 7(b), it appears that the dumbbell pore is coarsening at the expense of the small pores near the end of the dumbbell (marked with arrows) that are likely migrating toward and merging with it due to the temperature gradient as mentioned previously. Also, there are likely pores or individual vacancies below the spatial resolution of the

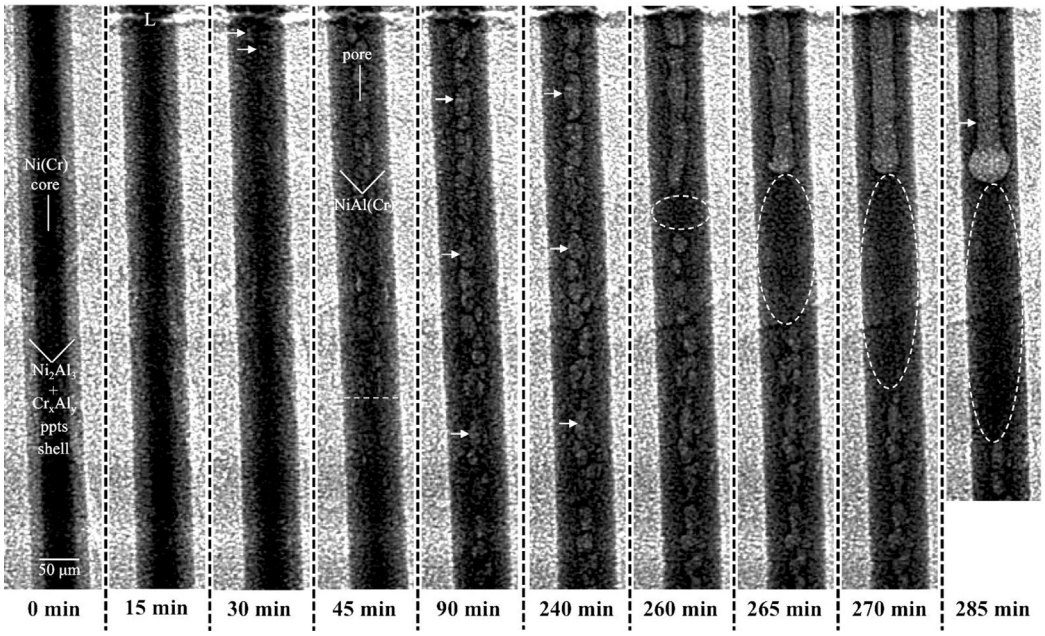

Fig. 4. Time evolution of 2D radiographs of the full FOV of the wire, all taken at the same angular position, starting from 0 min showing longitudinal pore evolution. The laser position is marked with an L.

tomographic imaging that are also migrating to the dumbbell, as it acts as a vacancy sink near the high temperature region of the sample. The grain boundaries visible in Fig. 7(c) indicate that grain boundary grooving has occurred within the wire at the pore surface, and that the grain size is much smaller than the wire diameter, i.e., that bamboo grains have not developed at the dumbbell. The grain boundaries may also provide a short-circuit diffusion path for vacancies to migrate to (and from) the dumbbell cavity.

To verify that the dumbbell formation was repeatable, a second sample was aluminized and annealed under the same conditions. The resultant projections are shown in Fig. 8, starting after 540 min of annealing, which is when the stagnant string of pores has already formed and begins to evolve due to the temperature gradient. The original location where the laser was impinging on the sample is marked with an L in the first projection in Fig. 8. However, the laser position was shifted after about 15 min at temperature, long before the stagnation point at 540 min, to the location indicated with an L′ where it remained for the duration of the experiment. In this case, the stagnation period was much longer than for the first sample; it increased by approximately 300 min. A similar progression as was

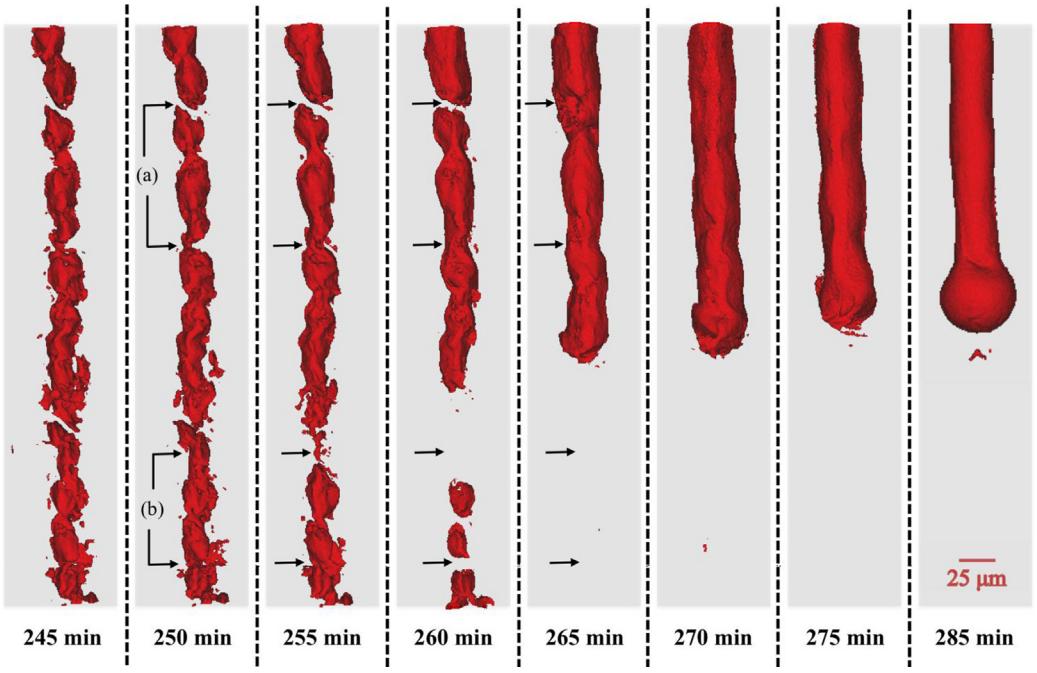

Fig. 5. Time evolution of 3D reconstructions at the same angular position showing pore (a) merging and (b) splitting events within the top half of the FOV between 245 and 285 min.

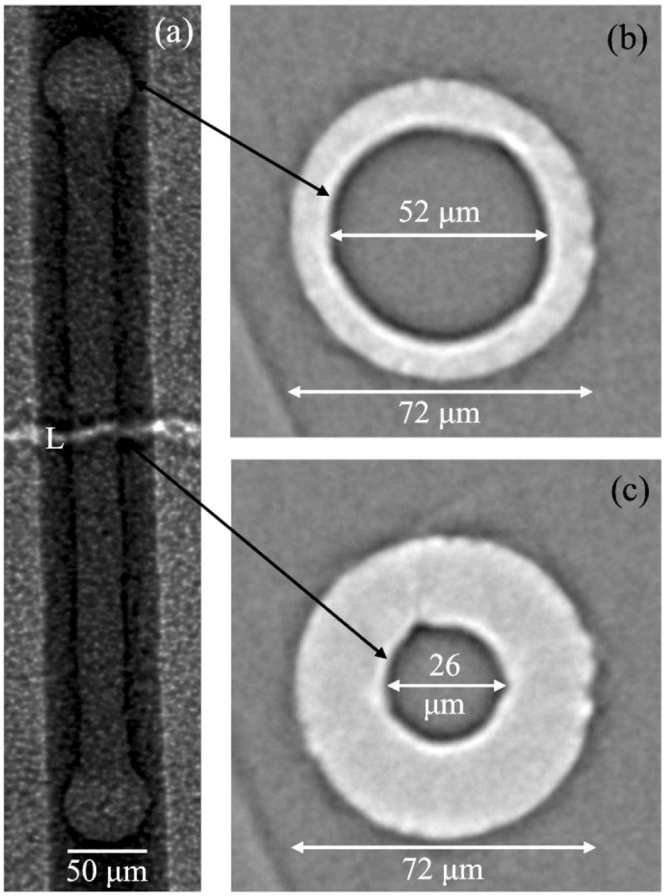

Fig. 6. (a) 2D radiograph of the dumbbell cavity formed within the wire after 285 min annealing and collected at room temperature after subsequent sample cooling, with reconstructed 2D cross-sections of (b) the spherical cap at its maximum diameter and (c) the middle section of the cylindrical shaft.

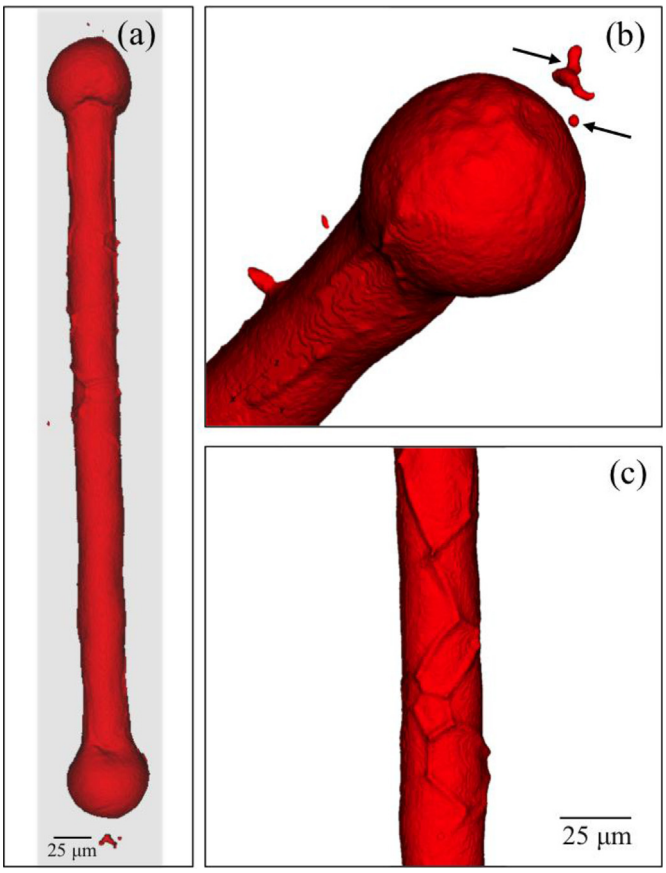

Fig. 7. 3D visualizations of (a) the full dumbbell cavity shown in Fig. 6(a) after 285 min annealing, (b) the bottom of the dumbbell with small satellite pores visible, and (c) the shaft of the dumbbell with grain boundaries on the surface.

shown in Fig. 4 is observed up until the point when the dumbbell forms. There are regions (marked with arrows) where the pore string splits during the merging process. After 570 min at temperature, a long, nearly-uniform cylinder has formed with a hemispherical cap, which grows into the larger spherical cap at the end of the cylinder by 585 min. Within another 5 min (590 min), the sphere becomes even more well-defined. The resultant pore structure appears very similar to what was observed at the end of the time sequence in Fig. 4.

To determine whether or not the dumbbell pore remains stable upon further annealing, the heat treatment was not interrupted and the experiment was continued as shown in Fig. 8. After another 5 min (595 min), the cavity connects to the wire surface near the top of the FOV (arrow). In addition, the cap on the bottom of the cylinder has elongated and the second end of the pore comes into view and has a hemispherical cap with the same diameter as the cylindrical portion. Thereafter, the wire fractures completely (indicated by the dotted white line), and the cylindrical portion of the cavity becomes unstable and rapidly disappears; the cap then pinches off and remains as a nearly spherical pore within the wire as shown in the 600 min projection. The last projection at 605 min shows that this pore is more spherical than the previous step and has decreased in volume. This sequence of events seems to indicate that the pore was gas-filled and that once the gas was released where the wire fractured, the cavity was able to sinter further. The overall diameter of the wire cross-section – approximately 72 μm measured at twelve different time steps between 0 and 285 min – does not change over time within the experimental error. This can be explained by the relatively small volume fraction of pores, between 3 and 4 vol.%, which was measured as a function of time over three different 140 μm sections from the top, middle, and bottom portions of the wire within the FOV. Furthermore, the volume expansion due to the formation of the pores is partially balanced by the molar volume decrease from the formation of the various intermetallic phases upon interdiffusion.

3.2.2. *Ex situ metallography experiments*

3.2.2.1. Microstructural features and evolution. To estimate the longitudinal temperature gradient and verify the results of the tomography study, several aluminized wires were annealed isothermally at 900, 1000, and 1100 °C and subsequently cross-sectioned for metallographic compositional and microstructural analysis. Fig. 9 shows a matrix of radial cross-sections annealed for three different times (15, 30, and 60 min) for (a) the reconstructed tomography slices from the top, middle, and bottom (corresponding to the high, medium, and low temperature regions, respectively) of the wire section presented in Fig. 4 and (b) a representative selection of optical micrographs of the wires annealed ex situ at 900, 1000, and 1100 °C for comparison. While the initial coating thickness remained constant from the top to the bottom of the wire section, the cross-sections in Fig. 9(a) clearly evolve at different rates, providing further evidence of the longitudinal temperature gradient. Based on the micrographs in Fig. 9(b), we expect the temperature gradient to be within the 900–1100 °C range.

To further investigate the microstructural evolution of the wires beyond 1 h, a series of wires was annealed at 1100 °C for up to 16 h

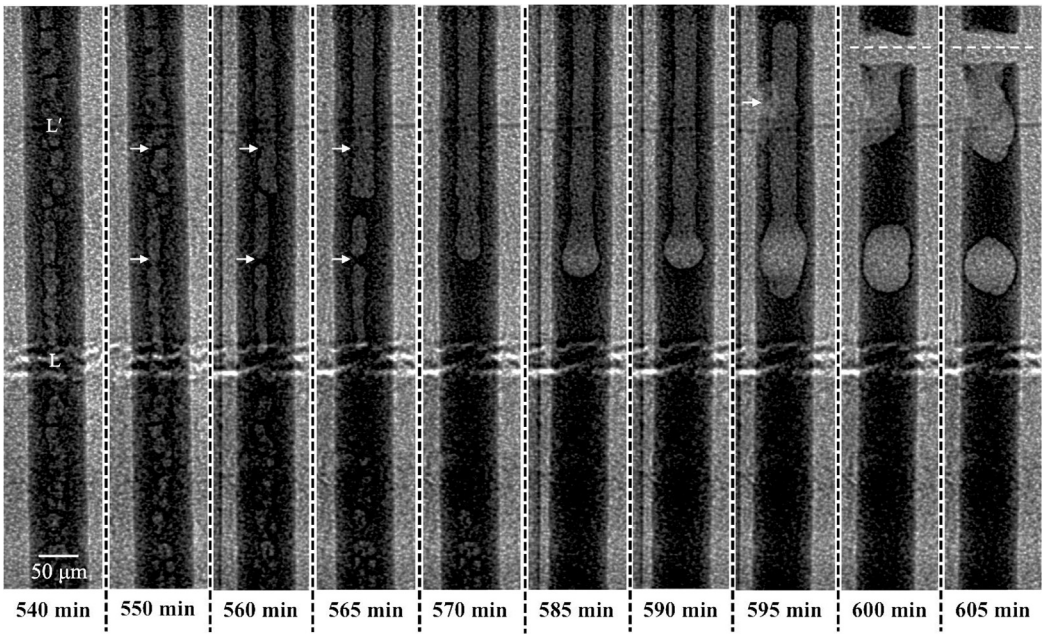

Fig. 8. Time evolution of the 2D radiographs of the full FOV of the wire, all taken at the same angular position, for a second sample showing the longitudinal pore evolution starting after 540 min of annealing.

as shown in Fig. 10. This temperature was chosen based on the relevant intrinsic diffusivities available in literature and the extensive Kirkendall porosity observed in the initial ex situ experiments. Because the characterization techniques used for the ex situ studies are destructive, the cross-sections shown in Fig. 10 are not from the same wire; hence they may have slightly different initial coating thicknesses and are therefore a less accurate representation of the microstructural evolution. However, several observations can still be made from this series of cross-sections. First, large cavities with crescent-shaped cross-sections have developed, as also observed in the tomographic reconstructions (Fig. 3). Also, certain features within the microstructure are observed in the ex situ cross-sections in Fig. 10 that were not distinguishable in the tomographic reconstructions. It is apparent that the Cr-rich precipitates that developed upon aluminization are still present in the outer layer and, in some cases, within the inner layer that has developed. These precipitates are most likely not seen in the tomographic reconstructions because there is minimal absorption contrast difference compared to the surrounding matrix and/or because they are smaller than the spatial resolution of the experiment. In addition, in Fig. 10, a two-phase β-NiAl(Cr) + α-Cr(Ni,Al) region near the center of the cross-sections is observed, which is likely the result of Cr rejection as the Ni(Cr) core is consumed by the NiAl(Cr) reaction layer. Similar α-Cr(Ni,Al) rejection was observed by Tu and Seigle in a Ni-25at.%Cr (Ni-23wt.%Cr) alloy aluminized in a 60 at.% (40.8 wt.%) Al pack for 8 h at 1000 °C [34]. Finally, in the cross-section annealed for 30 min shown in Fig. 10(b), a clear color difference can be seen between the bluish-gray outer region in contact with the pore and the remainder of the brownish cross-section. Based on the phase diagram and EDS, the bluish-gray region is Al-rich NiAl(Cr) and the brownish portion of the cross-section is Ni-rich NiAl(Cr). This suggests that the Ni_2Al_3 coating transforms to NiAl very quickly and that homogenization by diffusion is delayed by the presence of the pore, which interrupts and lengthens the diffusion path.

The cross-sections in Fig. 10(e) and (f) were annealed for 8 and 16 h, respectively, at 1100 °C. Both seem to be fully homogenized, but still contain Cr-rich precipitates that appear to be coarsening. The pores grew to the size shown in Fig. 10 during homogenization, and the crescent shape remained throughout the process. These cross-sections are representative of the wires annealed under isothermal conditions and are clearly different from the dumbbell-shaped pore observed in the tomography experiments, which again suggests that the temperature gradient was responsible for the unusual dumbbell shape. Based on the metallographic cross-sections, it appears that these pores are relatively stable, at least up to 16 h.

Once the Kirkendall pores form, they act as sinks for other vacancies in the system and continue to grow and merge into the pores with crescent-shaped cross-sections observed in both the tomography and ex situ experiments. Klinger et al. modeled the hollowing of a cylindrical core–shell nanowire and suggest that this crescent shape is a result of the combination of surface diffusion along the internal surfaces of the core and shell, diffusion at the core/shell interface, and diffusion along the grain boundaries in the shell [53]. Because surface, interface, and grain boundary diffusion are much faster than bulk diffusion at solid-state diffusion temperatures, these mechanisms should play a significant role in determining the shape and growth kinetics of the pores that form near the β-NiAl/γ-Ni(Cr) interface [53]. This also explains the observation made about Fig. 10(b) regarding the mitigation of homogenization diffusion in the outer wire region in contact with the pore. Because the pore forms near the β-NiAl/γ-Ni(Cr) interface, it interrupts the supply of Ni atoms directly from the core, thereby increasing the diffusion distance, and hence requiring a longer time for that region to homogenize.

In most cases the resultant hollow structure formed via this Kirkendall technique is single-phase. It has been suggested that ternary systems are not ideal for this method because they may result in an internally porous wire rather than the pores merging to form a tube [54]. A possible explanation is that, in a ternary system where the core material is an alloy or a compound, only one element outdiffuses significantly faster than the inward diffusion of the shell phase, which could lead to the formation of precipitates near the core that inhibit the pores from fully connecting [3]. In this case, due to the large amount of Cr in the Ni–Cr wire core, the wire remains two-phase following homogenization; hence the Cr-rich

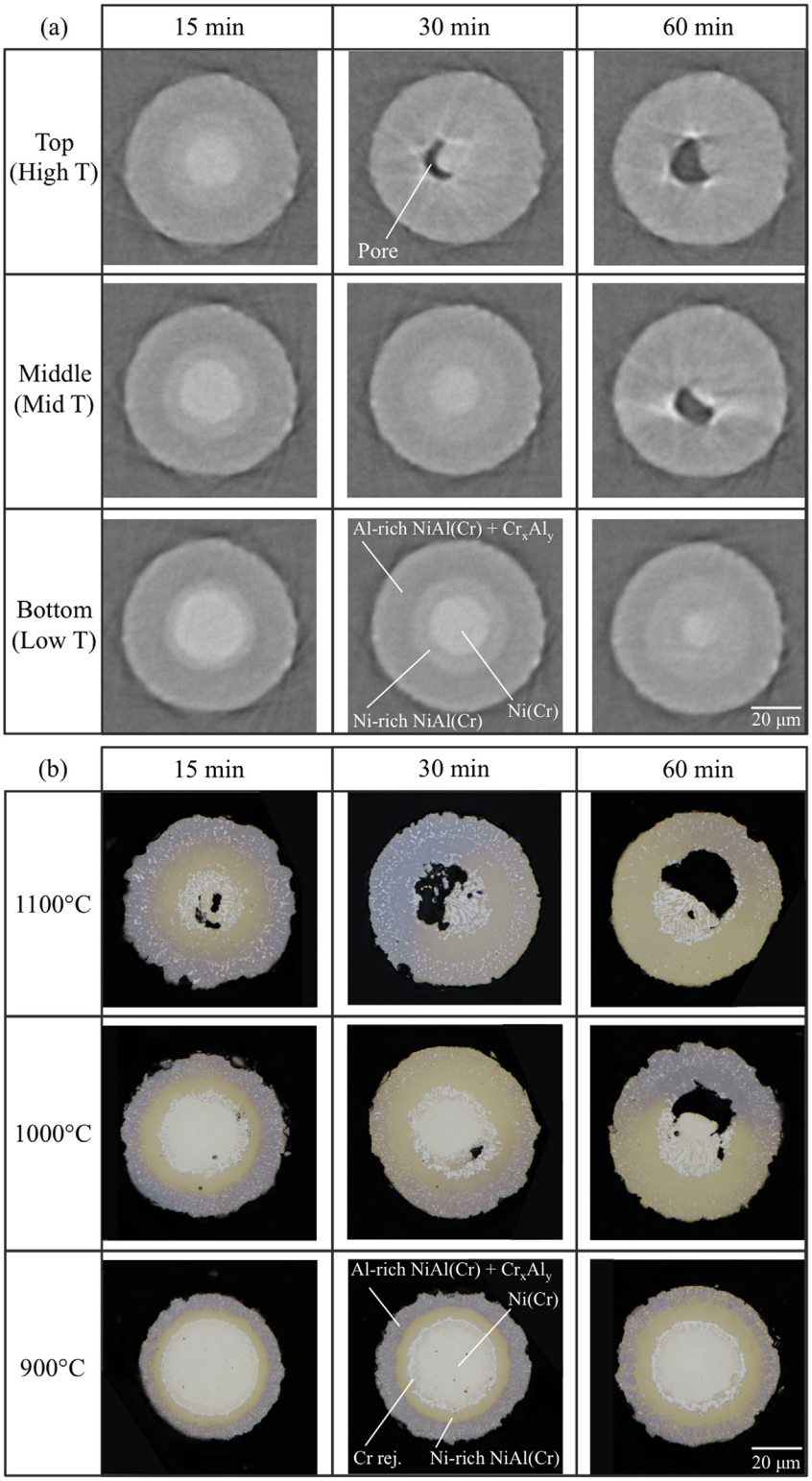

Fig. 9. Radial cross-section of aluminized Ni-20wt.%Cr wires annealed (a) in situ from the top, middle, and bottom of the field of view (corresponding to the high, medium, and low temperature regions, respectively) originally presented in Fig. 4 and (b) ex situ at 900, 1000, and 1100 °C for 15, 30, and 60 min.

precipitates may be impeding the growth of the pores. However, it is expected that the pores would eventually take a more circular shape in cross-section to minimize surface area, if given enough time.

3.2.2.2. Microstructure reproducibility. Multiple wires were aluminized and annealed at 1100 °C for 16 h to assess reproducibility. Fig. 11 shows optical micrographs of two cross-sections from each of three different aluminized wires, e.g., Fig. 11(a) and (b) are images

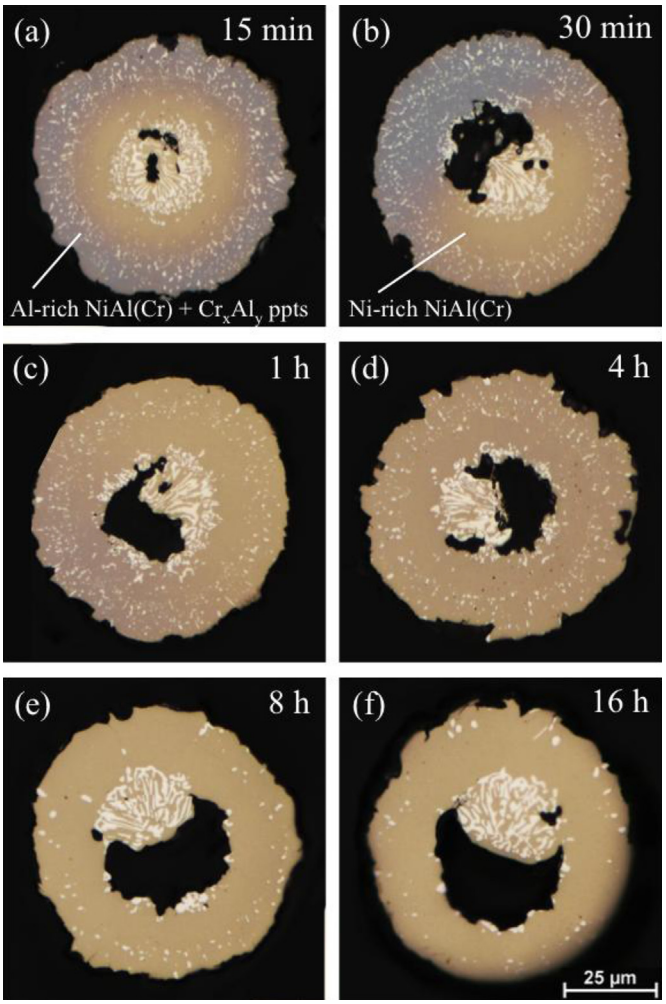

Fig. 10. Optical micrographs of typical aluminized wire cross-sections following isothermal annealing at 1100 °C for a) 15 min, b) 30 min, c) 1 h, d) 4 h, e) 8 h, and f) 16 h. The edge damage is due to metallographic preparation.

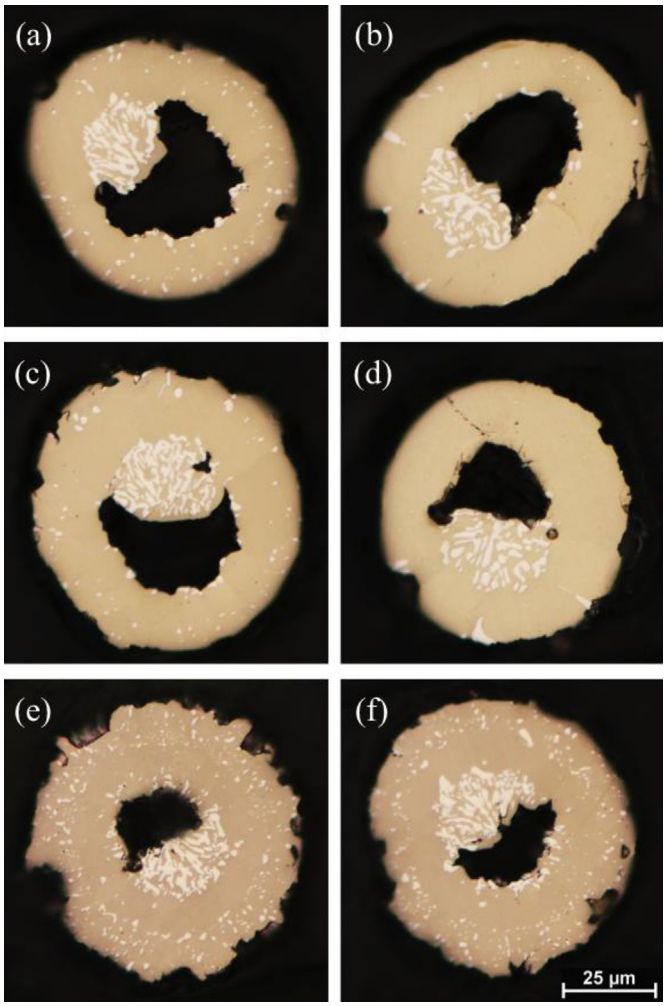

Fig. 11. Optical micrographs of typical aluminized wire cross-sections following isothermal annealing at 1100 °C for 16 h. Pairs of cross-sections - (a) and (b), (c) and (d), and (e) and (f) - were taken from three different wires.

taken from different regions within the same wire located 1–5 mm apart (about 20–100 times the wire diameter). All six cross-sections look similar in terms of phase constituents and pore shape, with some variation with respect to pore and Cr precipitate area fraction. Also, the color of the NiAl(Cr) matrix phase is slightly different between wires, but appears to be similar between the two cross-sections from the same wire. These discrepancies are likely due to the fact that the initial coating layer thickness varies slightly between the three wires. Therefore, the overall compositions are somewhat different, which accounts for the slight variation in phase fraction and matrix phase color.

To test this hypothesis, the compositions of these six cross-sections were measured via EDS and plotted on the ternary isotherm (constructed at 1150 °C [55], 50 °C above our annealing temperature) as shown in Fig. 12. Each symbol indicates a different wire: the solid and hollow square symbols correspond to measurements collected from the cross-sections in Fig. 11(a) and (b), respectively, the circles represent Fig. 11(c) and (d) and the triangles denote compositions for the cross-sections in Fig. 11(e) and (f). The three colors each represent composition data collected from different regions of the cross-sections. The blue symbols correspond to the overall wire composition as determined from one large area scan that contained the entire cross-section. These data points are all within the two-phase B2–NiAl(Cr) + fcc-Cr(Ni,Al) region, near the B2 phase region as expected based on the contrast and area fraction of precipitates observed in the images. The overall Al composition ranges from about 32 to 42 at.%, with the cross-sections shown in Fig. 11(e) and (f) having the highest Al content. The Cr content ranges from approximately 12 to 16 at.% and the Ni content from 45 to 52 at.%. These values appear to correspond well with the observations made based on the image contrast. Each of the red symbols represents the average of five point measurements conducted within the matrix phase. For all six cross-sections, they fall on the NiAl(Cr) phase boundary, indicating that this is the equilibrium composition and will hence not evolve further. Finally, the green symbols represent data collected from the central region of the cross-sections containing a high area fraction of the Cr-rich precipitates. Because these precipitates are too small for accurate analysis via EDS and often difficult to distinguish in the SEM, the data points plotted are average values from six rectangular areas containing both the Cr-rich precipitates and the matrix phase. Therefore, these points do not accurately represent the Cr-rich precipitates and should shift to the Cr solid solution phase boundary if the contribution from the matrix phase is excluded. The composition data set presented here agrees well with the phase constituent results previously discussed and suggests that phase distribution and pore formation is repeatable in different wires and relatively consistent within the same wire.

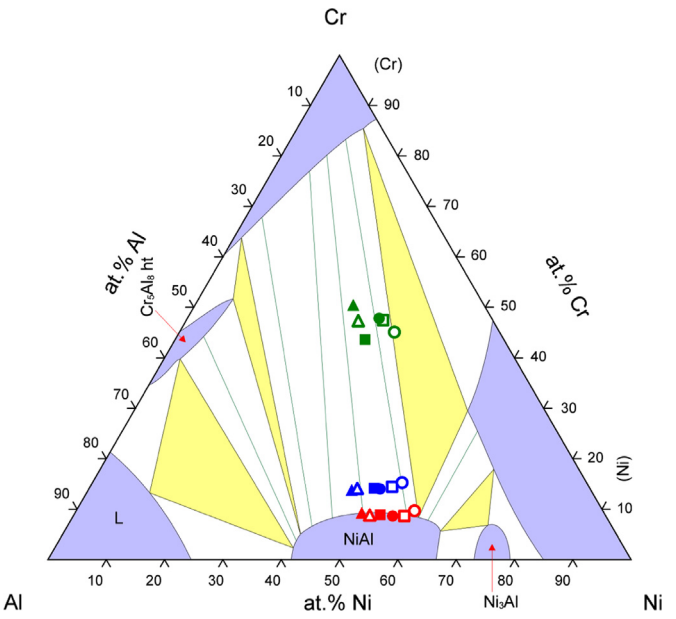

Fig. 12. Isothermal section at 1150 °C of the Ni–Cr–Al ternary phase diagram [59] with average wire (blue) or phase (red and green) compositions plotted for the six cross-sections (annealed at 1100 °C) shown in Fig. 10. The square symbols correspond to (a) and (b), circle symbols to (c) and (d), and triangular symbols to (e) and (f). Solid symbols represent (a), (c) and (e) while hollow symbols represent (b), (d) and (f), respectively. (For interpretation of the references to colour in this figure legend, the reader is referred to the web version of this article.)

3.2.2.3. Summary of microstructure and pore evolution mechanisms. These results highlight the advantages of using a combination of tomographic microscopy and traditional metallography as tools for understanding interdiffusion – tomography is nondestructive and provides a means to capture time-resolved, in situ evolution of phenomena in a single sample, while metallography provides more detailed snapshots of the evolution and fills in the information missing from dynamic experiments. Based on a combination of the observations made in both sets of experiments, a schematic of the multistep microstructural evolution is presented in Fig. 13. The microstructure evolves from (1) the as-coated aluminized Ni–20Cr wire as follows: (2) a NiAl(Cr) reaction layer starts growing while rejecting Cr, and a dominant Kirkendall pore forms near the γ-Ni(Cr)/β-NiAl(Cr) interface; (3) the reaction layer continues to grow at the expense of the core, further rejecting Cr, and the pore acts as a vacancy sink and grows via core surface, core/shell interface, and grain boundary diffusion; (4) the core is nearly consumed, the pore cross-section has become crescent-shaped, and homogenization is impeded in the region behind the pore because of the lengthening diffusion distance due to the presence of the pore; (5) the pore continues to grow by completely consuming the core, but is prevented from becoming circular due to the presence of the Cr precipitates near the center, and the shell is still not fully homogenized in the region behind the pore; (6) finally, the fully homogenized NiAl(Cr) + Cr(Al,Ni) two-phase structure with an internal central pore with a crescent-shaped cross-section develops. A precipitate-free NiAl(Cr) layer seems to develop initially because of the relatively high solubility limit of Cr, 10 at.% at 1150 °C, but as it grows the excess Cr is rejected in the form of precipitates, creating the two-phase microstructure near the core. The Cr-rich precipitates formed in the as-coated shell remain stable, as Ni_2Al_3 has a very limited solubility for Cr, until the shell transforms into NiAl(Cr) and the precipitates are then able to dissolve and/or coarsen.

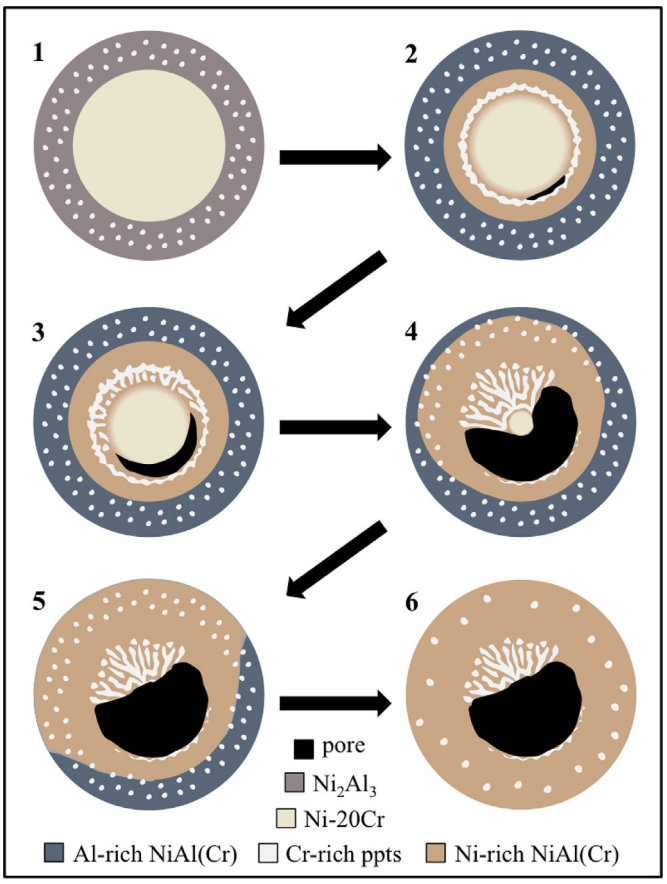

Fig. 13. Schematic showing multistep evolution of (1) the as-coated aluminized Ni–20Cr wire to (6) the fully homogenized NiAl(Cr) + Cr(Al,Ni) two-phase microstructure containing a central pore with a crescent-shaped cross-section.

4. Conclusions

The pack cementation coating method, which is well-established to coat bulk objects, was used here to form ~10 μm thick nickel aluminide coatings on Ni-20wt.%Cr wires with 50 μm original diameter. Upon annealing, two phenomena were observed: (i) diffusion reaction and phase evolution and (ii) Kirkendall pore formation and evolution. The following conclusions are reached:

a. In situ X-ray tomographic microscopy was performed on a wire subjected to a longitudinal temperature gradient imposed by laser-based heating.
   1. Kirkendall pores nucleate in the β-NiAl(Cr) layer that rapidly replaces the as-deposited Ni_2Al_3 shell. The pore cross-sections initially form crescent shapes near the β-NiAl(Cr)/γ-Ni(Cr) interface and then grow to 10–25 μm diameter as they serve as vacancy sinks.
   2. A stagnant string of pores forms along the entire length of wire and further evolves due to the presence of a temperature gradient. Pores migrate to the hot zone and coalesce into a dumbbell-shaped cavity positioned symmetrically about the hottest location.
   3. Upon further annealing of a second sample containing a dumbbell cavity, the wire fractured and the pore became unstable and sintered.

b. Isothermal ex situ experiments were performed on a series of wires annealed at 1100 °C that were examined metallographically.

4. The above mechanisms of phase and pore formation active during interdiffusion are confirmed. However, the dumbbell-shaped cavities were not observed, implying that a temperature gradient is needed to create them.
5. Compositional analysis via EDS showed that the equilibrium phases after full homogenization are a NiAl(Cr) matrix containing fine Cr-rich precipitates which were not distinguishable in the tomographic reconstructions.
6. Cavities with crescent-shaped cross-sections appear to form due to surface, interface, and grain boundary diffusion mechanisms and do not spheroidize after 16 h at 1100 °C, most likely because the Cr precipitate formation near the center of the cross-sections inhibits further pore evolution.

Acknowledgments

AEPyP acknowledges the National Science Foundation Graduate Research Fellowship Program for funding support. The authors acknowledge the financial support from the Defense Advanced Research Projects Agency under award number W91CRB1010004 (Dr. Judah Goldwasser, program manager). They also thank Profs. Peter Voorhees and David Seidman (Northwestern University) for their helpful discussions, Mr. Matt Glazer (Northwestern University) for experimental assistance at SLS, and Mr. Ashwin Shahani (Northwestern University) for assistance with the MATLAB script for measuring pore volume fraction. JLF also acknowledges the CCMX and PSI for funding.

References

[1] A.D. Smigelskas, E.O. Kirkendall, Zinc diffusion in alpha brass, Trans. AIME 171 (1947) 130–142.
[2] F. Seitz, On the porosity observed in the Kirkendall effect, Acta Metall. 1 (1953) 355–369.
[3] H.J. Fan, U. Gösele, M. Zacharias, Formation of nanotubes and hollow nanoparticles based on Kirkendall and diffusion processes: a review, Small 3 (2007) 1660–1671, http://dx.doi.org/10.1002/smll.200700382.
[4] K. Zeng, R. Stierman, T.C. Chiu, D. Edwards, K. Ano, K.N. Tu, Kirkendall void formation in eutectic SnPb solder joints on bare Cu and its effect on joint reliability, J. Appl. Phys. 97 (2005), http://dx.doi.org/10.1063/1.1839637.
[5] H. Schröder, K. Samwer, U. Köster, Micromechanism for metallic-glass formation by solid-state reactions, Phys. Rev. Lett. 54 (1985) 197–200, http://dx.doi.org/10.1103/PhysRevLett.54.197.
[6] Z. Radi, P.B. Barna, J. Lábár, Kirkendall voids and the formation of amorphous phase in the Al-Pt thin-film system prepared by high-temperature successive deposition, J. Appl. Phys. (1996) 4096, http://dx.doi.org/10.1063/1.361772.
[7] Y. Yin, R.M. Rioux, C.K. Erdonmez, S. Hughes, G.A. Somorjai, A.P. Alivisatos, Formation of hollow nanocrystals through the nanoscale Kirkendall effect, Science 80 (304) (2004) 711–714.
[8] H.-P. Liang, Y.-G. Guo, H.-M. Zhang, J.-S. Hu, L.-J. Wan, C.-L. Bai, Controllable AuPt bimetallic hollow nanostructures, Chem. Commun. (Camb) (13) (2004) 1496–1497, http://dx.doi.org/10.1039/b402745k.
[9] S. Zhou, B. Varughese, B. Eichhorn, G. Jackson, K. McIlwrath, Pt-Cu core-shell and alloy nanoparticles for heterogeneous NOx reduction: anomalous stability and reactivity of a core-shell nanostructure, Angew. Chem. 117 (2005) 4615–4619, http://dx.doi.org/10.1002/ange.200500919.
[10] Q. Li, R.M. Penner, Photoconductive cadmium sulfide hemicylindrical shell nanowire ensembles, Nano Lett. 5 (2005) 1720–1725, http://dx.doi.org/10.1021/nl050994x.
[11] H. Jin Fan, M. Knez, R. Scholz, K. Nielsch, E. Pippel, D. Hesse, et al., Monocrystalline spinel nanotube fabrication based on the Kirkendall effect, Nat. Mater 5 (2006) 627–631, http://dx.doi.org/10.1038/nmat1673.
[12] H. Tan, S. Li, W.Y. Fan, Core – shell and hollow nanocrystal formation via small molecule surface photodissociation; Ag@Ag_2Se as an example, J. Phys. Chem. B 110 (2006) 15812–15816, http://dx.doi.org/10.1021/jp0616011.
[13] C. Hwee, B. Ng, H. Tan, W.Y. Fan, Formation of Ag_2Se nanotubes and dendrite-like structures from UV Irradiation of a CSe_2/Ag colloidal solution, Langmuir. 22 (2006) 9712–9717.
[14] J. Zhou, J. Liu, X. Wang, J. Song, R. Tummala, N.S. Xu, et al., Vertically aligned Zn_2SiO_4 nanotube/ZnO nanowire heterojunction arrays, Small 3 (2007) 622–626, http://dx.doi.org/10.1002/smll.200600495.
[15] X. Chen, Z. Zhang, Z. Qiu, C. Shi, X. Li, Hydrothermal fabrication and characterization of polycrystalline linneite (Co_3S_4) nanotubes based on the Kirkendall effect, J. Colloid Interface Sci. 308 (2007) 271–275, http://dx.doi.org/10.1016/j.jcis.2006.12.054.
[16] Y. Chang, M.L. Lye, H.C. Zeng, Large-scale synthesis of high-quality ultralong copper nanowires, Langmuir 21 (2005) 3746–3748, http://dx.doi.org/10.1021/la050220w.
[17] Q. Wang, J.X. Li, G.D. Li, X.J. Cao, K.J. Wang, J.S. Chen, Formation of CuS nanotube arrays from CuCl Nanorods through a gas-solid reaction route, J. Cryst. Growth 299 (2007) 386–392, http://dx.doi.org/10.1016/j.jcrysgro.2006.11.304.
[18] F. Aldinger, Controlled porosity by an extreme Kirkendall effect, Acta Metall. 22 (1974) 923–928.
[19] H.J. Fan, R. Scholz, F.M. Kolb, M. Zacharias, U. Gösele, Growth mechanism and characterization of zinc oxide microcages, Solid State Commun. 130 (2004) 517–521, http://dx.doi.org/10.1016/j.ssc.2004.03.014.
[20] L. Ye, C. Wu, W. Guo, Y. Xie, MoS_2 hierarchical hollow cubic cages assembled by bilayers: one-step synthesis and their electrochemical hydrogen storage properties, Chem. Commun. (Camb) 2 (2006) 4738–4740, http://dx.doi.org/10.1039/b610601c.
[21] C. Guo, G. Zhang, Z. Shen, P. Sun, Z. Yuan, Q. Jin, et al., Hydrothermal synthesis and formation mechanism of micrometer-sized MoO_2 hollow spheres, Chin. J. Chem. Phys. 19 (2006) 543–548, http://dx.doi.org/10.1360/cjcp2006.19(6).543.6.
[22] M.K. Allison, G. Hawkins, Pack cementation, Gen. Electr. Rev. 17 (1914) 947–951.
[23] R. Mévrel, C. Duret, R. Pichoir, Pack cementation processes, Mater. Sci. Technol. 2 (1986) 201–206, http://dx.doi.org/10.1179/026708386790123297.
[24] H. Choe, D.C. Dunand, Synthesis, structure, and mechanical properties of Ni-Al and Ni-Cr-Al superalloy foams, Acta Mater. 52 (2004) 1283–1295, http://dx.doi.org/10.1016/j.actamat.2003.11.012.
[25] F.S. Nogorani, F. Ashrafizadeh, A. Saatchi, Microstructural analysis and growth mechanism of single-step aluminum-titanium diffusion coatings on a nickel-based substrate, Surf. Coatings Technol. 210 (2012) 97–102, http://dx.doi.org/10.1016/j.surfcoat.2012.08.071.
[26] D. Erdeniz, K.W. Sharp, D.C. Dunand, Transient liquid-phase bonded 3D woven Ni-based superalloys, Scr. Mater. 108 (2015) 60–63, http://dx.doi.org/10.1016/j.scriptamat.2015.06.016.
[27] J. Li, C. Xia, Y. Gu, Effect of temperature on microstructure of molybdenum diffusion coating on titanium substrate, J. Cent. South Univ. Technol. 11 (2004) 15–18, http://dx.doi.org/10.1007/s11771-004-0003-8.
[28] C. Wang, D.C. Dunand, Concurrent growth of Kirkendall pores and vapor – solid – solid protuberances on Ni wires during Mo vapor-phase deposition, Metall. Mater. Trans. A 45A (2014) 6252–6259, http://dx.doi.org/10.1007/s11661-014-2587-4.
[29] C. Wang, D.C. Dunand, Microstructure evolution during Al, Ti, and Mo surface deposition and volume diffusion in Ni-20Cr wires and Woven structures, Metall. Mater. Trans. A 46 (2015) 2249–2254, http://dx.doi.org/10.1007/s11661-015-2794-7.
[30] D. Erdeniz, D.C. Dunand, Microstructure development during pack aluminization of nickel and nickel-chromium wires, Intermetallics 50 (2014) 43–53, http://dx.doi.org/10.1016/j.intermet.2014.02.009.
[31] G.W. Goward, L.W. Cannon, Pack cementation coatings for superalloys: a review of history, theory, and practice, J. Eng. Gas. Turbines Power 110 (1988) 150, http://dx.doi.org/10.1115/1.3240078.
[32] G.W. Goward, D.H. Boone, Mechanisms of formation of diffusion aluminide coatings on nickel-base superalloys, Oxid. Met. 3 (1971) 475–495, http://dx.doi.org/10.1007/BF00604047.
[33] R. Pichoir, Influence of the Mode of Formation on the Oxidation and Corrosion Behavior of NiAI-type Protective Coatings, in: Mater. Coatings to Resist High Temp. Corros, Applied Science Publisher, London, 1978, pp. 271–292.
[34] A.J. Hickl, R.W. Heckel, Kinetics of phase layer growth during aluminide coating of nickel, Metall. Trans. A 6 (1975) 431–440, http://dx.doi.org/10.1007/BF02658400.
[35] D.K. Das, V. Singh, S. V Joshi, Evolution of aluminide coating microstructure on nickel-base cast superalloy CM-247 in a single-step high-activity aluminizing process, Metall. Mater. Trans. A 29A (1998) 2173–2188.
[36] D.C. Tu, L.L. Seigle, Kinetics of formation and microstructure of aluminide coatings on Ni-Cr alloys, Thin Solid Films 95 (1982) 47–56.
[37] S.R. Levine, R.M. Caves, Thermodynamics and kinetics of pack aluminide coating formation on IN-IO0, J. Electrochem. Soc. 121 (1974) 1051–1064.
[38] R. Bianco, R.A. Rapp, Pack Cementation Diffusion Coatings, in: Metall. Ceram. Prot. Coatings, Chapman & Hall, London, 1996, pp. 236–260.
[39] M.M.P. Janssen, G.D. Rieck, Reaction diffusion and Kirkendall-effect in the nickel-aluminum system, Trans. AIME 239 (1967) 1372–1385.
[40] F. Aldinger, M. Kuhn, Isotropic growth in diffusion samples of aluminium and nickel with rotational symmetry, Z. Für Met. 22 (1975).
[41] A.M. Hodge, D.C. Dunand, Synthesis of nickel–aluminide foams by pack-aluminization of nickel foams, Intermetallics 9 (2001) 581–589, http://dx.doi.org/10.1016/S0966-9795(01)00047-4.
[42] T. Philippe, D. Erdeniz, D.C. Dunand, P.W. Voorhees, A phase-field study of the aluminizing of nickel, Philos. Mag. 95 (2015) 935–947, http://dx.doi.org/10.1080/14786435.2015.1010622.
[43] L. Zhao, S. Ha, K.W. Sharp, A.B. Geltmacher, R.W. Fonda, H. Alex, et al., Permeability measurements and modeling of topology-optimized metallic 3-D woven lattices, Acta Mater. 81 (2014) 326–336, http://dx.doi.org/10.1016/j.actamat.2014.08.037.
[44] J.L. Fife, M. Rappaz, M. Pistone, T. Celcer, G. Mikuljan, M. Stampanoni, Development of a laser-based heating system for in situ synchrotron-based X-ray tomographic microscopy, J. Synchrotron Radiat. 19 (2012) 352–358, http://dx.doi.org/10.1107/S0909049512003287.

[45] F. Marone, M. Stampanoni, Regridding reconstruction algorithm for real-time tomographic imaging, J. Synchrotron Radiat. 19 (2012) 1029–1037, http://dx.doi.org/10.1107/S0909049512032864.
[46] C.A. Schneider, W.S. Rasband, K.W. Eliceriri, NIH Image to image J: 25 years of image analysis, Nat. Methods 9 (2012) 671–675.
[47] H. Childs, E. Brugger, B. Whitlock, J. Meredith, S. Ahern, D. Pugmire, et al., VisIt: an end-user tool for visualizing and analyzing very large data, in: High Perform. Vis. Extrem. Sci. Insight, 1, 2012, pp. 357–372.
[48] T. Chart, A. Dinsdale, F. Putland, The NPL ALLOYDATA bank: its use in the calculation of phase diagrams for super-alloy development, Spec. Publ. Soc. (34) (1980) 235–245.
[49] C.J. Smithells, C.E. Ransley, The diffusion of gases through metals III - the degassing of nickel and the diffusion of carbon monoxide through nickel, Proc. R. Soc. A 155A (1936) 195–212.
[50] D.A. Woodford, Gas phase embrittlement and time dependent cracking of nickel based superalloys, Energy Mater. 1 (2006) 59–79, http://dx.doi.org/10.1179/174892306X99679.
[51] S.Y. Hu, C.H. Henager Jr., Phase-field simulation of void migration in a temperature gradient, Acta Mater. 58 (2010) 3230–3237, http://dx.doi.org/10.1016/j.actamat.2010.01.043.
[52] K. Deckelnick, C.M. Elliott, G. Dziuk, Computation of geometric partial differential equations and mean curvature flow, Acta Numer. 14 (2005) 139–232, http://dx.doi.org/10.1017/S0962492904000224.
[53] L. Klinger, O. Kraft, E. Rabkin, A model of Kirkendall hollowing of core–shell nanowires and nanoparticles controlled by short-circuit diffusion, Acta Mater. 83 (2015) 180–186, http://dx.doi.org/10.1016/j.actamat.2014.09.050.
[54] S. Prasad, A. Paul, Theoretical consideration on the formation of nanotube following the Kirkendall effect, Appl. Phys. Lett. 90 (2007) 233114, http://dx.doi.org/10.1063/1.2747184.
[55] N.C. Oforka, B.B. Argent, Thermodynamics of Ni-Cr-Al alloys, J. Less Common Met. 114 (1985) 97–109.